UC Berkeley
UC Berkeley Previously Published Works

Title
Direct localization and delineation of human pedunculopontine nucleus based on a self-supervised magnetic resonance image super-resolution method

Permalink
https://escholarship.org/uc/item/7z79x6mc

Journal
Human Brain Mapping, 44(9)

ISSN
1065-9471

Authors
Li, Jun
Guan, Xiaojun
Wu, Qing
et al.

Publication Date
2023-06-15

DOI
10.1002/hbm.26311

Peer reviewed

RESEARCH ARTICLE

WILEY

Direct localization and delineation of human pedunculopontine nucleus based on a self-supervised magnetic resonance image super-resolution method

Jun Li[1] 🟢 | Xiaojun Guan[2] | Qing Wu[1] | Chenyu He[1] 🟢 | Weimin Zhang[1] | Xiyue Lin[1] | Chunlei Liu[3,4] | Hongjiang Wei[5,6] | Xiaojun Xu[2] 🟢 | Yuyao Zhang[1,7]

[1]School of Information Science and Technology, ShanghaiTech University, Shanghai, China

[2]Department of Radiology, The Second Affiliated Hospital, Zhejiang University School of Medicine, Hangzhou, China

[3]Department of Electrical Engineering and Computer Science, University of California at Berkeley, Berkeley, California, USA

[4]Helen Wills Neuroscience Institute, University of California at Berkeley, Berkeley, California, USA

[5]School of Biomedical Engineering, Shanghai Jiao Tong University, Shanghai, China

[6]Institute of Medical Robotics, Shanghai Jiao Tong University, Shanghai, China

[7]Ihuman Institute, ShanghaiTech University, Shanghai, China

Correspondence
Yuyao Zhang, School of Information Science and Technology, ShanghaiTech University, 393 Middle Huaxia Road, 201210, Shanghai, China.
Email: zhangyy8@shanghaitech.edu.cn

Xiaojun Xu, Department of Radiology, The Second Affiliated Hospital, Zhejiang University School of Medicine, 88 Jiefang Road, 310009, Hangzhou, Zhejiang, China.
Email: xxjmailbox@zju.edu.cn

Abstract

The pedunculopontine nucleus (PPN) is a small brainstem structure and has attracted attention as a potentially effective deep brain stimulation (DBS) target for the treatment of Parkinson's disease (PD). However, the in vivo location of PPN remains poorly described and barely visible on conventional structural magnetic resonance (MR) images due to a lack of high spatial resolution and tissue contrast. This study aims to delineate the PPN on a high-resolution (HR) atlas and investigate the visibility of the PPN in individual quantitative susceptibility mapping (QSM) images. We combine a recently constructed Montreal Neurological Institute (MNI) space unbiased QSM atlas (MuSus-100), with an implicit representation-based self-supervised image super-resolution (SR) technique to achieve an atlas with improved spatial resolution. Then guided by a myelin staining histology human brain atlas, we localize and delineate PPN on the atlas with improved resolution. Furthermore, we examine the feasibility of directly identifying the approximate PPN location on the 3.0-T individual QSM MR images. The proposed SR network produces atlas images with four times the higher spatial resolution (from 1 to 0.25 mm isotropic) without a training dataset. The SR process also reduces artifacts and keeps superb image contrast for further delineating small deep brain nuclei, such as PPN. Using the myelin staining histological atlas as guidance, we first identify and annotate the location of PPN on the T1-weighted (T1w)-QSM hybrid MR atlas with improved resolution in the MNI space.

Jun Li and Xiaojun Guan contributed equally to this study.

Then, we relocate and validate that the optimal targeting site for PPN-DBS is at the middle-to-caudal part of PPN on our atlas. Furthermore, we confirm that the PPN region can be identified in a set of individual QSM images of 10 patients with PD and 10 healthy young adults. The contrast ratios of the PPN to its adjacent structure, namely the medial lemniscus, on images of different modalities indicate that QSM substantially improves the visibility of the PPN both in the atlas and individual images. Our findings indicate that the proposed SR network is an efficient tool for small-size brain nucleus identification. HR QSM is promising for improving the visibility of the PPN. The PPN can be directly identified on the individual QSM images acquired at the 3.0-T MR scanners, facilitating a direct targeting of PPN for DBS surgery.

1 | INTRODUCTION

The pedunculopontine nucleus (PPN) is a collection of heterogeneous neurons situated at the junction of the midbrain and pons (Jenkinson et al., 2009), located right below the red nucleus (RN) dorsally to the substantia nigra (SN) and extends caudally ∼5–10 mm to the level of the locus coeruleus (Hamani et al., 2016). It displays substantial reciprocal connectivity with the spinal cord and the brain cortex through the basal ganglia and thalamus (Aravamuthan et al., 2007; Garcia-Gomar et al., 2022; Muthusamy et al., 2007). The PPN plays a crucial role in various motor functions, such as voluntary limb movements and locomotion, states of arousal, and providing sensory feedback to the cerebral cortex (Jenkinson et al., 2009; Leiras et al., 2022; Thevathasan et al., 2018). PPN is also a potentially effective target in deep brain stimulation (DBS) surgeries to treat levodopa-refractory gait and balance disturbances in some patients with Parkinson's disease (PD) or other movement disorders (Cury et al., 2022; Dayal et al., 2021; Galazky et al., 2018; Thevathasan et al., 2018).

Studies indicate that the direct targeting method can improve the targeting accuracy of the neurosurgery (Fenoy & Schiess, 2018; Tonge et al., 2016). However, PPN-DBS surgeries mostly rely on the indirect targeting method (Goetz et al., 2019) due to the unsatisfactory imaging effect of PPN. The identification of PPN based on non-invasive imaging techniques has previously been performed on 7.0-T ultrahigh-field magnetic resonance imaging (MRI) scanners using the MP2RAGE sequence (Cong et al., 2018; Wang et al., 2019) and on a 1.5-T MRI scanner using proton-density MRI protocol (Zrinzo et al., 2008). In the studies based on 7.0-T MR scanners, the authors benefited from the relatively high-resolution (HR; $0.7 \times 0.7 \times 0.7$ mm^3 isotropic) gray matter (GM) enhanced T1-weighted (T1w) image to identify PPN from the surrounding white matter (WM) structures (Cong et al., 2018; Wang et al., 2019). Nevertheless, due to the reticular nature of the mesencephalic locomotor region where PPN is embedded (Cury et al., 2022), and the low signal-to-noise ratio (SNR) of HR isotropic

MR images, the PPN border presented by MP2RAGE images was ambiguous. In Zrinzo and colleagues' study, the proton-density MR image was fused with T1w image to enhance the GM-WM image contrast (Zrinzo et al., 2008). However, limited by the image resolution and image contrast provided by the 1.5-T MR scanner, only the superior cerebellar peduncle (SCP), central tegmental tracts, and lemniscal system were identified using stereotactic atlas as guidance; then, the location of PPN was inferred from the WM structures. Inspired by these previous works, we hypothesize that two essential conditions are required for achieving a direct visualization of PPN, demanding high spatial resolution and high tissue contrast, for example, between GM and WM. Clear contrast between PPN and its surrounding WM fiber bundles at high image resolution is necessary.

Quantitative susceptibility mapping (QSM) has been developed to enable quantitative investigations of tissue compositions due to susceptibility differences between tissues (Li et al., 2011; Liu et al., 2015; Shmueli et al., 2009; Wei et al., 2015; Wei, Cao, et al., 2019). Due to the high sensitivity to iron and myelin content in the brain tissue, QSM can provide superior imaging contrast between paramagnetic iron-rich deep brain GM and the surrounding diamagnetic WM structures (Dimov et al., 2018; Kerl et al., 2012; Sun et al., 2015). It has been shown to facilitate the depiction of iron-rich DBS targeting nuclei and sub-nuclei from the surrounding WM structures, for example, the subthalamic nucleus (Alkemade et al., 2017; Liu et al., 2013), globus pallidus internus (Wei, Zhang, et al., 2019), sub-nuclei of the thalamus (Li et al., 2019; Yu, Li, et al., 2021; Yu, Ren, et al., 2021; Zhang et al., 2018), and the dentate nucleus of the cerebellum (He et al., 2017). A previous study using 7.0-T MRI susceptibility-weighted imaging of the non-human primate brainstem indicated that PPN shows higher susceptibility than its adjacent WM structures, such as the SCP and the lemniscal system (Zitella et al., 2015). Thus, QSM may be a proper imaging technique to support a direct visualization of the human PPN surrounded by WM structures (Alho et al., 2017; Pahapill & Lozano, 2000).

In this study, we combine a recently constructed Montreal Neurological Institute (MNI) space unbiased QSM atlas (MuSus-100) (C. He et al., 2022), with a self-supervised deep learning image super-resolution (SR) technique to achieve a clear delineation of PPN on the atlas with improved spatial resolution. The MuSus-100 QSM atlas was constructed from 100 subjects' images at 3.0-T and provided superior SNR and image contrast compared to individual images. Inspired by a multiple-image MRI SR method (Wu et al., 2021), we adopt an implicit neural representation (INR) network to achieve a self-supervised arbitrary up-scaling rate image SR process (Wu et al., 2023). The INR-based SR process overcomes the image resolution limitation for the 3.0-T MR atlas, and minimizes the artifact and blurring effects into the super-resolved image, which are significant drawbacks of the conventional interpolation technique (e.g., trilinear, sinc). We perform the proposed image SR method on the MuSus-100 atlas to improve the spatial resolution of the QSM template from 1 mm isotropic to 0.25 mm isotropic. Then guided by a myelin staining histology human brain atlas (Martin, 2012), we localize and delineate PPN on the atlas with improved spatial resolution. We also examine the feasibility of directly identifying the approximate PPN location on the 3.0-T individual QSM MR images of PD patients and healthy young adults. Although 7.0-T MR scanners provide relatively higher image resolution, methods under 3.0-T scanners donate opportunities for broader clinical applications.

2 | METHODS

2.1 | Workflow of this study

The MNI-space unbiased QSM atlas MuSus-100 (He et al., 2022) is obtained from GitHub (https://github.com/SMILE-Lab-ShanghaiTech/MuSus-100_Atlas). As shown in Figure 1, the T1w and QSM templates with resolution $1 \times 1 \times 1$ mm^3 were used for deriving a HR T1w-QSM hybrid atlas, on which the PPN region was identified and delineated. In terms of application, we relocated the optimal targeting site of PPN-DBS as proposed by a recent study (Goetz et al., 2019) based on the defined PPN spatial location in MNI space. Furthermore, the visibility of PPN was examined in individual QSM images of 10 patients with PD and 10 healthy young adults. Finally, we examined the feasibility of aligning our PPN delineation onto individual images via the registration of the MuSus-100 T1w-atlas and the individual T1w images to locate the PPN on the individual images.
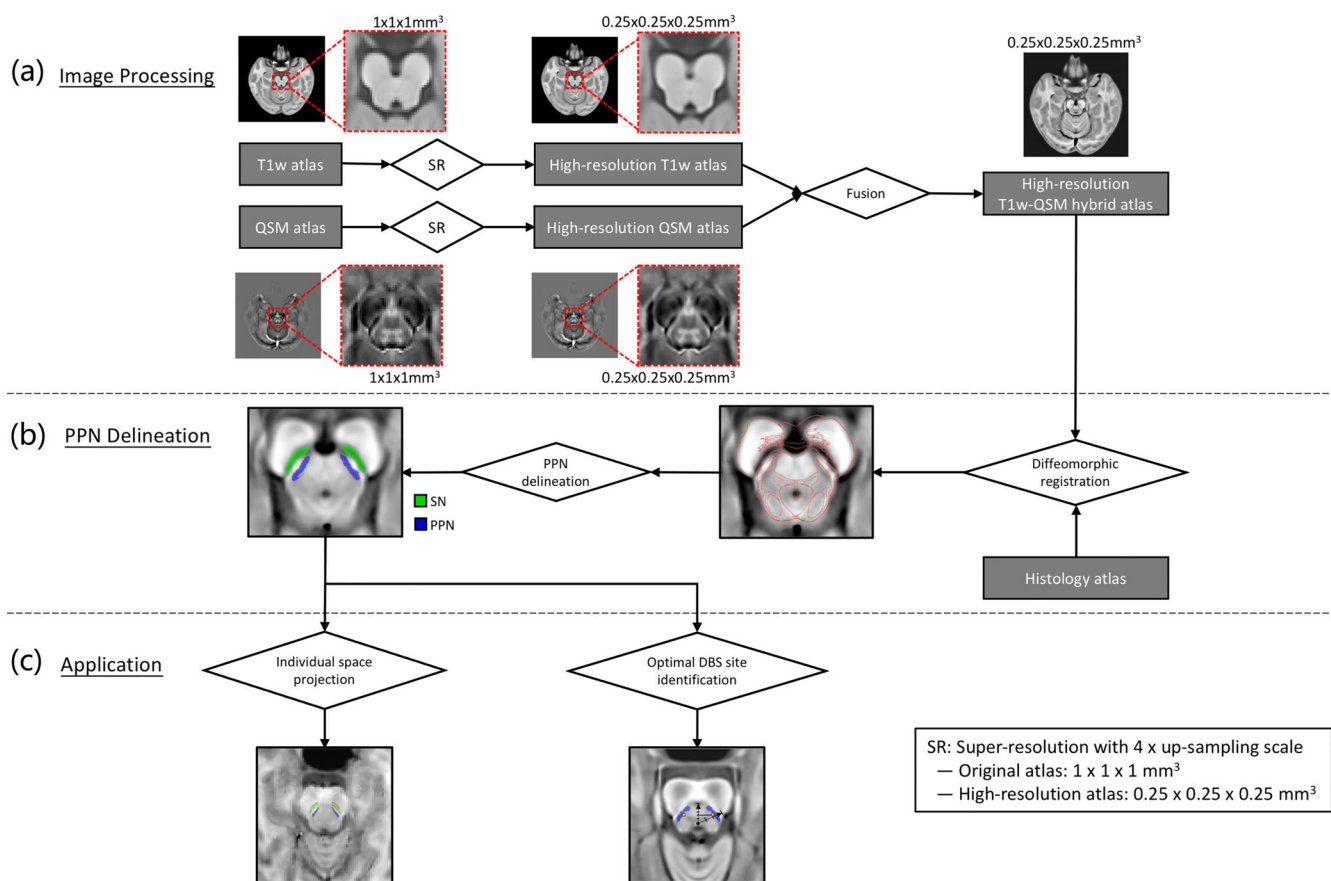

FIGURE 1 Workflow of the study. The major steps of the present study include (a) high-resolution T1w-QSM hybrid atlas creation, (b) delineation of PPN, and (c) demonstration of potential clinical application. DBS, deep brain stimulation; PPN, pedunculopontine nucleus; QSM, quantitative susceptibility mapping; SN, substantia nigra; SR, super-resolution; T1w, T1-weighted.

2.2 | Atlas resolution improvement via INR-based SR algorithm

In the method of INR-based SR network, the desired HR image is modeled by an implicit function of the 3D spatial coordinate, and the LR image is considered as the discrete sampling of the function. Therefore, the up-sampling task is to learn the implicit function from a limited LR observation using a deep, fully connected network with position encoding (Tancik et al., 2020). Since the spatial coordinates are continuous, once the function is well estimated, the HR image with an arbitrary resolution can be reconstructed. The proposed method consists of a position encoding (Tancik et al., 2020) and an 18-layer fully connected network with dense connections. More details about the network architecture can be found in an online article (Wu et al., 2023).

The pipeline of the proposed self-supervised SR method is conducted in two stages (Figure S1): (a) Model Training: An LR grid is extracted from a given LR image. Then, the intensity of each voxel coordinate $\mathbf{p} = (x,y,z)$ of the LR grid is embedded using position encoding $\gamma(\mathbf{p}) = [\cos(2\pi\mathbf{Bp}), \sin(2\pi\mathbf{Bp})]^T$, where each element in $\mathbf{B} \in \mathbb{R}^{L \times 3}$ and L is the dimension of position encoding, and fed to a multilayer perceptron (MLP) neural network to produce the estimated voxel intensity $\hat{I}_{lr}(\mathbf{p})$ at the coordinate $\mathbf{p}$. Afterward, the MLP can be optimized using a back-propagation to minimize the mean squared loss error (MSE loss) between the estimated voxel intensity $\hat{I}_{lr}(\mathbf{p})$ and the real observed voxel intensity $I_{lr}(\mathbf{p})$. (b) HR image reconstruction: The well-trained SR model is considered an approximator of the implicit function for the voxel intensity of the given LR image. Therefore, it can generate an HR image with an arbitrary resolution. In the present study, we reduced the voxel size from 1 mm isotropic to 0.25 mm isotropic, which means the HR image has 64 times as many voxels as the LR image. Then, we assigned the intensity to each voxel coordinate $\mathbf{p} = (x,y,z)$ of the HR grid according to the trained SR model to produce the voxel intensity $\hat{I}_{hr}(\mathbf{p})$. Thus, an HR image up-sampled from the LR image was obtained.

2.3 | HR T1w-QSM hybrid atlas generation

The T1w-QSM hybrid atlas, on which the PPN region was then manually delineated using an aligned histology atlas as guidance (Figure 1b), is generated from the HR templates. The HR T1w-QSM hybrid atlas is obtained via a linear intensity fusion of T1w and QSM templates: Intensity$_{hybrid}$ = Intensity$_{T1w}$ − α × Intensity$_{QSM}$, using the "Image Calculator" module of the toolbox for data processing and analysis for brain imaging toolbox (http://rfmri.org/dpabi) (Yan et al., 2016). Since the QSM atlas shows higher contrast among the brainstem structures but shows a less clear outer boundary of the brainstem than the T1w atlas, we tried multiple α values ranging from 7500 to 25,000 with an incremental step of 2500 to obtain an appropriate hybrid atlas.

2.4 | Alignment of histology atlas based on myelin-stained sections with hybrid atlas

The outlines of the histology atlas based on the myelin-stained sections (Martin, 2012) were aligned with three slices of our hybrid atlas using the open-source software of ImageJ (version 2.1.0/1.53c, https://imagej.net/software/fiji/; Schindelin et al., 2012). First, three slices containing the region of PPN in the axial, sagittal, and coronal views, respectively, were taken from our hybrid atlas. Then, dozens of anchor points, mainly including the points on the boundaries of the anatomical structures (e.g., outlines of the brainstem, SN, medial lemniscus, and SCP and decussation), were manually marked on both the outlines of the histology atlas and our hybrid atlas by an experienced radiologist. Finally, the outlines of the histology atlas were aligned with the slices of our hybrid atlas based on the marked anchor points using the function of "Big Warp" implemented in ImageJ (https://imagej.net/plugins/bigwarp). The locations of the PPN region and the structures nearby (i.e., the SCP and decussation, medial lemniscus, RN, and SN) were indicated on both atlases.

2.5 | Regions of interest segmentation

The atlases were inspected using ITK-SNAP software (version 3.8.0, http://www.itksnap.org/pmwiki/pmwiki.php). The PPN region was manually delineated by the radiologists on the HR hybrid atlas slice by slice in the axial directions using the software of ITK-SNAP, based on the myelin-stained sections and the priori knowledge of the anatomical location of PPN. Besides the PPN, the SN, and RN were also delineated for reference.

2.6 | Relocating an optimal DBS site of PPN

The targeting site of PPN-DBS with optimal treatment effect based on the relative coordinates was proposed in a recent study (Goetz et al., 2019). The optimal target for PPN-DBS is located at the junction of two lines respectively perpendicular to two-thirds of the brainstem normalized laterality (Xbn) and to two-fifths of the brainstem normalized antero-posteriority (Ybn), on the level of ponto-mesencephalic junction. We relocated this optimal site in our proposed PPN delineation to visualize its anatomical location.

2.7 | Direct visualization of PPN on individual images at 3.0-T Magnetic fields

To examine whether the location of PPN can be identified on individual QSM images, we further inspected individual images of 10 patients diagnosed with PD and 10 healthy young adults using ITK-SNAP. The individual images of PD patients and healthy young adults were acquired at the Second Affiliated Hospital, Zhejiang University School of Medicine. The imaging parameters are presented in Table S1. All procedures of the present study follow the Declaration of Helsinki, and were approved by the Ethics Committee of the Second Affiliated

Hospital, Zhejiang University School of Medicine. The participants provided written informed consent before participating in this study.

The contrast ratio of the difference between the signals of PPN and adjacent medial lemniscus versus the signal of PPN was calculated from a representative slice of each modality to quantitatively compare the image contrast in delineating PPN from the surrounding tissues, by the equation: $\text{Contrast ratio} = |\text{Sig}_{PPN} - \text{Sig}_{ML}| / |\text{Sig}_{PPN}|$, where Sig_{PPN} and Sig_{ML} represent the mean signal intensities of the selected region of PPN and the medial lemniscus, respectively. A higher contrast ratio suggests that the PPN region is more delineable from its adjacent structures.

2.8 | Delineation of PPN on individual images via registration of T1w-atlas and images

The QSM is not a clinically routine imaging modality, which needs to be reconstructed from the GRE phase image (Schweser et al., 2011). Thus, we also examined the feasibility of PPN identification via the registration of the MuSus-100 T1w-atlas and the individual T1w images (Figure 1c). The PPN region delineated on the hybrid atlas was aligned onto the individual images by the registration of the T1w-atlas and individual T1w images using two alignment methods for comparison: (1) the linear approach of affine registration function of ITK-SNAP, with mutual information as the image similarity metric (Andres & Isoardi, 2007) and (2) the nonlinear approach of Diffeomorphic Anatomical Registration Through Exponentiated Lie Algebra (DARTEL) (Ashburner, 2007) with SPM12 toolbox (https://www.fil.ion.ucl.ac.uk/spm/software/spm12/). For validation, two radiologists manually segmented the PPN region on the individual QSM images. The consistency between the aligned PPN region and the manually segmented PPN region was validated using the Dice coefficient: $2 \times |\text{PPN}_{aligned} \cap \text{PPN}_{manual}| / (|\text{PPN}_{aligned}| + |\text{PPN}_{manual}|)$. Moreover, the contrast ratio of the difference between the signals of the aligned PPN region and adjacent medial lemniscus versus the signal of PPN was also examined on a representative slice of each modality.

2.9 | Statistical analysis of brain tissue contrast

One-way analysis of variance (IBM SPSS Statistics, version 22) was used to compare the contrast ratios of the PPN region and the surrounding tissues among different MR image modalities. An Independent two-sample t-test was used as the post hoc test to further reveal the contrast-ratio differences between every two modalities. A statistically significant level was set at $p < .05$.

3 | RESULTS

3.1 | Comparison between HR template images generated via the proposed SR model and conventional interpolation methods

The interpolation using the trilinear or fifth-order B-splines methods was performed by the SimpleITK library (https://simpleitk.org/) of

Python. We select an enlarged patch in a representative axial slice that contains PPN and SN to compare the HR image generation performance of our SR model with different interpolation methods (Figure 2). As emphasized via the arrows in both T1w and QSM images, the trilinear interpolation and fifth-order B-splines introduce fluctuation-like artifacts to varying degrees. We draw two profile lines to indicate image details in the generated HR QSM images. As shown in Figure 2, lower-right panel, the image intensity variation in Profile Line 1 demonstrates the most severe periodic + intensity fluctuations produced in the trilinear HR image. The degree of such fluctuations is reduced but cannot be neglected in the fifth-order B-splines interpolation. The intensity fluctuations in interpolation methods are typically brought by the sinc interpolation kernel, while the profile line extracted from our SR model shows the smoothest intensity-varying range in the selected region. We can also notice the difference in intensity in Profile Line 2 at the eighth voxel (as highlighted with a vertical dotted line). The susceptibility produced by our SR model is slightly different from those generated by the other methods (e.g., the voxel shows paramagnetic susceptibility by the SR method but diamagnetic susceptibility by the other methods). Such difference is also caused by the smoother variation produced by the implicit function-based SR method. As shown in Figure 2, upper-right panel, intensity clustering is conducted using a k-means clustering model in Python (https://www.python.org/) on a representative patch to demonstrate the potential effect of image intensity smoothness on image segmentation. As highlighted by the arrows, the proposed SR method induces smooth and clear boundaries in-between different brain tissues.

3.2 | HR T1w-QSM hybrid atlas generation

A representative axial slice of the T1w atlas and QSM atlas is presented in the first column of Figure S2a. As presented, the QSM atlas provides images with clearer contrast and a sharp tissue border for distinguishing detailed brainstem structures than that in the T1w atlas. However, the outer boundary of the brainstem in the QSM atlas is not as clear as that in the T1w atlas. As shown in the highlighted part (curves with gray bounding boxes in the background) of image intensity profile line plots (Figure S2b), different values of α within the interval [7500 and 25,000] are used for hybrid image fusion. When $\alpha = 17,500$, the intensity plots show relatively sharp slopes for both the tissue border of PPN and the outer boundary of the brainstem, indicating the clearest tissue border contrast. Thus, we generate the T1w-QSM hybrid atlas with a scalar $\alpha = 17,500$ that controls the contribution proportion of QSM contrast in the hybrid atlas at an appropriate level.

3.3 | Delineation of PPN region on the T1w-QSM atlas

The hybrid atlas was referenced to the outline of the myelin-stained sections (Martin, 2012) to identify the PPN region (Figure 3). The PPN region is surrounded by WM with higher signal intensity, such as the
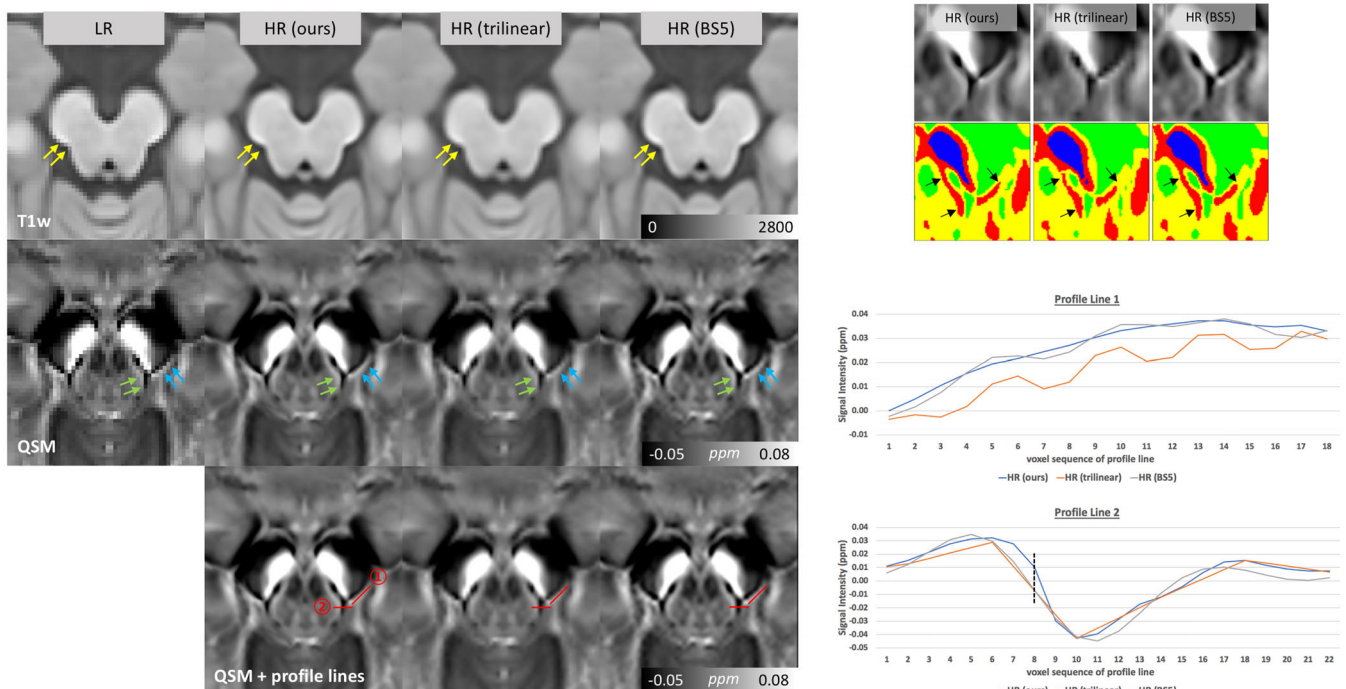
FIGURE 2 A visual comparison of HR images obtained by the proposed SR model and different interpolation methods. On the left panel, the slice views of the brainstem on the T1w atlas and QSM atlas are illustrated for the HR images obtained by the proposed SR model and different interpolation methods, including the trilinear method and the fifth-order B-splines method. The yellow arrows denote the boundary of the brainstem on the T1w images. The green arrows denote the PPN region. The blue arrows denote the vein beside the brainstem tissue. The signal intensity of three profile lines of the HR QSM images is shown on the lower-right panel. The intensity clustering result by the k-means method on a representative patch containing the brainstem is shown on the upper-right panel. The differences in the boundaries of small brainstem structures segmented by k-means are denoted by the black arrows. BS5, fifth-order B-splines; HR, high-resolution; LR, low-resolution; ppm, parts per million; SR, super-resolution.

decussation of the SCP and the medial lemniscus. Enlarged views of PPN and its surroundings in axial, sagittal, and coronal directions are presented on slices with 1 or 2-mm spatial intervals (Figure 4). As shown, the PPN (in blue) shows lower signal values than its adjacent structures on the hybrid atlas, which is located medially to the medial lemniscus and laterally to the decussation SCP. A three-dimensional (3D) view of the PPN region is also shown to demonstrate the PPN location in the brain (Figure S3). The approximate extent of the PPN region spans from 12 mm to 21 mm rostral to Point B (i.e., the intersection of a line tangential to the floor of the fourth ventricle and a line passing through the fastigium and perpendicular to the first line) (Cong et al., 2018; Zrinzo et al., 2008), from 4.5 to 9.5 mm lateral to the midline, and 0.5 to 9.5 mm anterior to Point B. Besides the PPN, other brainstem structures showing differentiated contrast with the surrounding tissues are annotated in detail on three selected slices (rostral, middle, and caudal PPN; Figure S4).

## 3.4 | Illustration of optimal targeting site of PPN-DBS on the PPN atlas

Goetz and colleagues proposed that the optimal target for PPN-DBS located at the junction of two lines respectively perpendicular to two-thirds of the brainstem normalized laterality (Xbn) and to two-fifths of the brainstem normalized antero-posteriority (Ybn), on the level of ponto-mesencephalic junction (Goetz et al., 2019). We identify this proposed optimal site and validate that this optimal target is at the middle-to-caudal part of PPN on our atlas (Figure 5).

3.5 | Direct visualization of PPN on individual images at 3.0-T Magnetic fields

The location of the PPN is identified on the QSM image and the hybrid image of a representative patient (Figure 6). The axial slice views of a representative section containing the caudal part of the PPN of all the 10 PD patients are illustrated (Figure S5). As shown, the PPN region can be identified from its surroundings on QSM images and hybrid images. The contrast ratios of the difference between the signal intensity of PPN and the adjacent medial lemniscus versus the signal intensity of PPN are 0.049 ± 0.014, 0.100 ± 0.014, 8.825 ± 2.780, and 0.260 ± 0.025, respectively, in the T1w, T2w, QSM, and hybrid images of the PD patients. A significant effect is revealed by one-way analysis of variance ($F = 8.825$, $p = .016$; Figure 7a), indicating that PPN is more delineable on the QSM and hybrid images. Besides the cohort of PD patients, the PPN region can

(a) Axial slice view
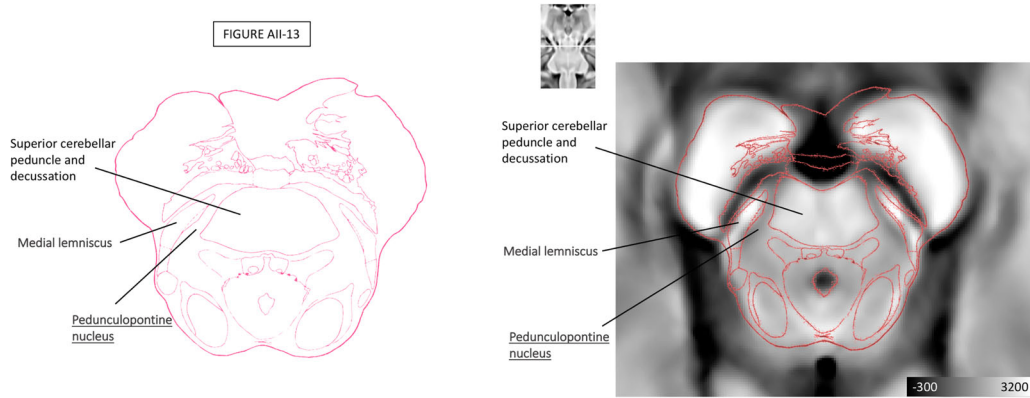
(b) Sagittal slice view
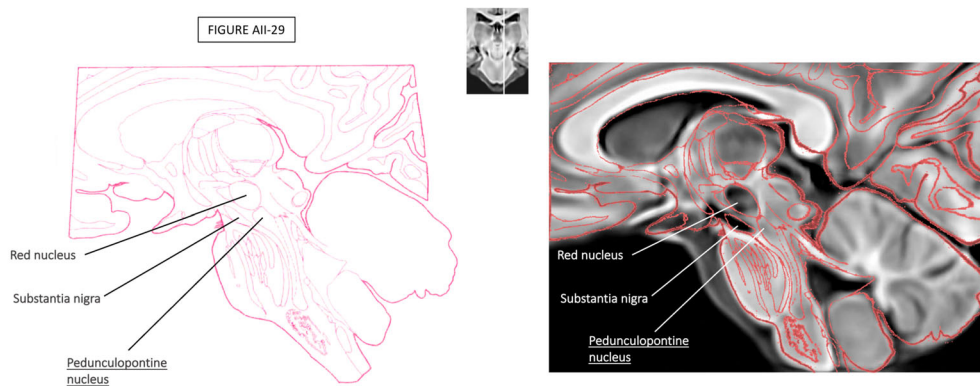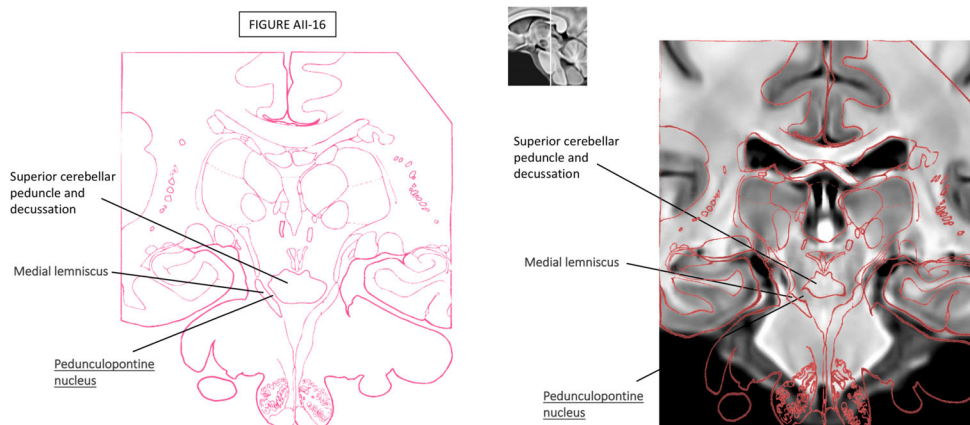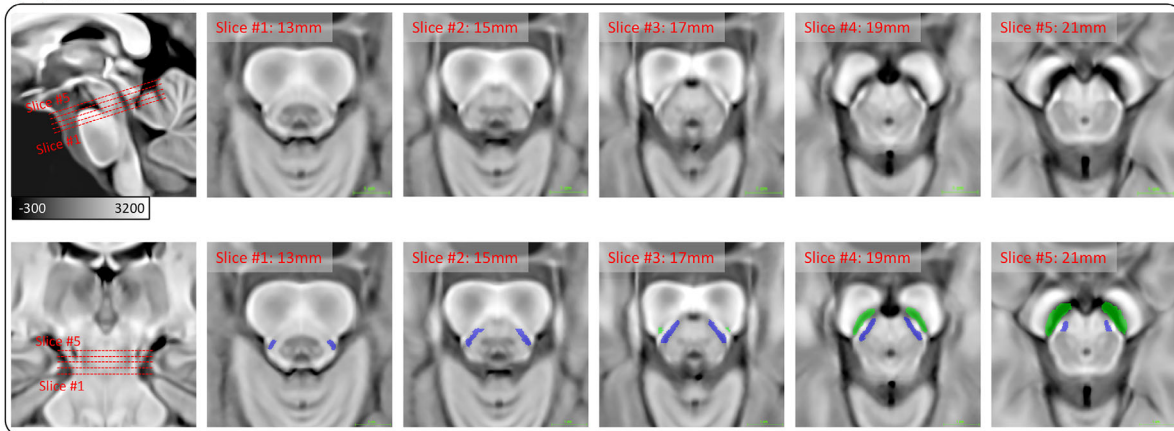

(c) Coronal slice view

FIGURE 3 Slices from T1w-QSM hybrid atlas referenced to myelin-stained sections. (a) Axial, (b) sagittal, and (c) coronal slice views of the T1w-QSM hybrid atlas (right column) compared with the outline (in red) extracted from the myelin-stained sections (Martin, 2012). The PPN region and its adjacent structures are indicated.

also be identified in the individual QSM images of healthy young adults (Figure S6).

The feasibility of PPN identification via the registration of the MuSus-100 T1w-atlas and the individual T1w images was also examined. The aligned PPN region on the individual space was visually confirmed on the individuals' QSM images, and also compared with the PPN region manually segmented on individual QSM images by two radiologists (Figure 8). There is an overlap between the aligned
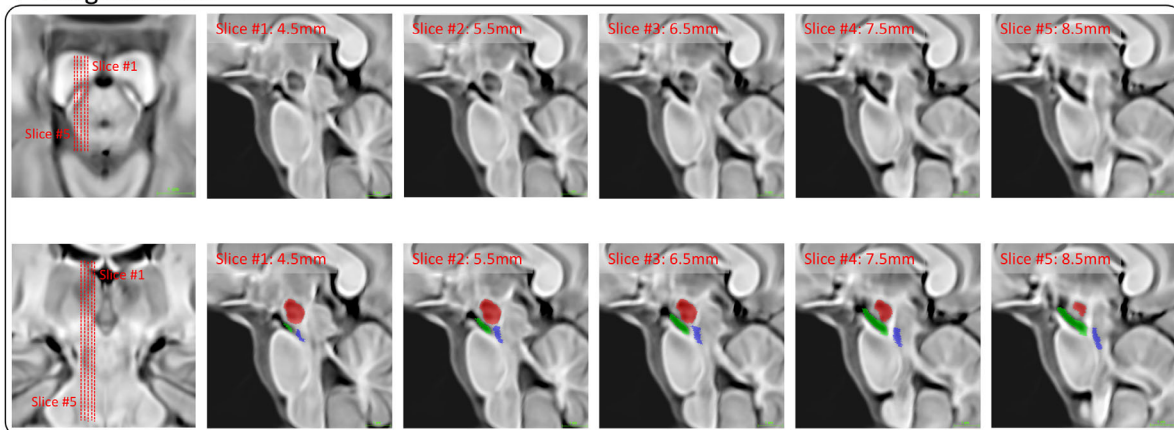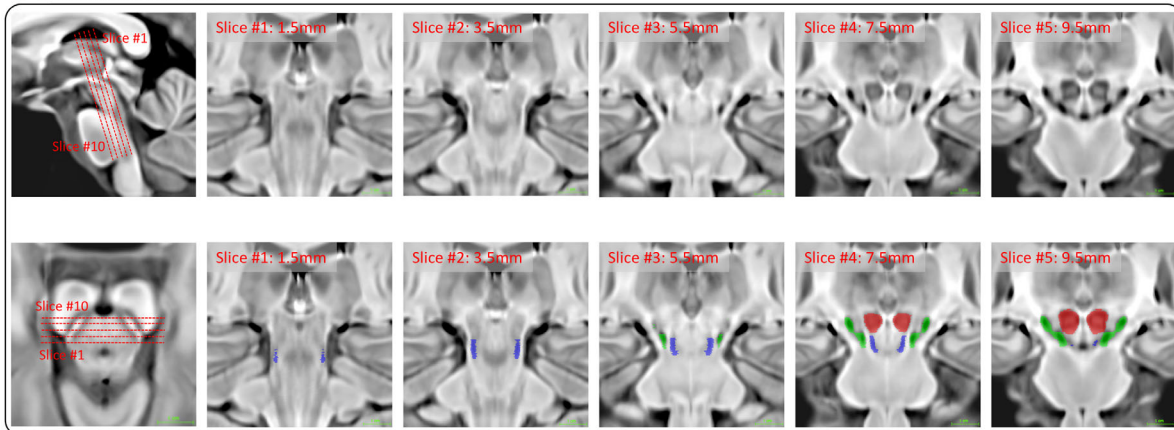
FIGURE 4 Slice views illustrating the PPN region. The PPN region is presented in (a) axial, (b) sagittal, and (c) coronal slice views. The interval between slices is 1 mm for the axial and coronal slice views and 0.5 mm for the sagittal view. The coordinates span from 13 to 21 mm rostral to point B for axial slice views, from 4.5 to 8.5 mm lateral to the midline for sagittal slice views, and from 1.5 to 9.5 mm anterior to point B for coronal slice views. The PPN region is in blue. The SN (in green) and RN (in red) are also delineated for reference. The position of point B is illustrated in Figure 5. PPN, pedunculopontine nucleus; RN, red nucleus; SN, substantia nigra.

PPN and the manually segmented PPN in all of the individuals, and the mean Dice coefficients are 0.487 and 0.505 by using the affine and DARTEL alignment methods, respectively (Table S2). Moreover,

the contrast ratios of the difference between the signal intensity of the aligned PPN and the adjacent medial lemniscus versus the signal intensity of PPN are 0.032 ± 0.007, 0.046 ± 0.008, 10.282 ± 7.681,
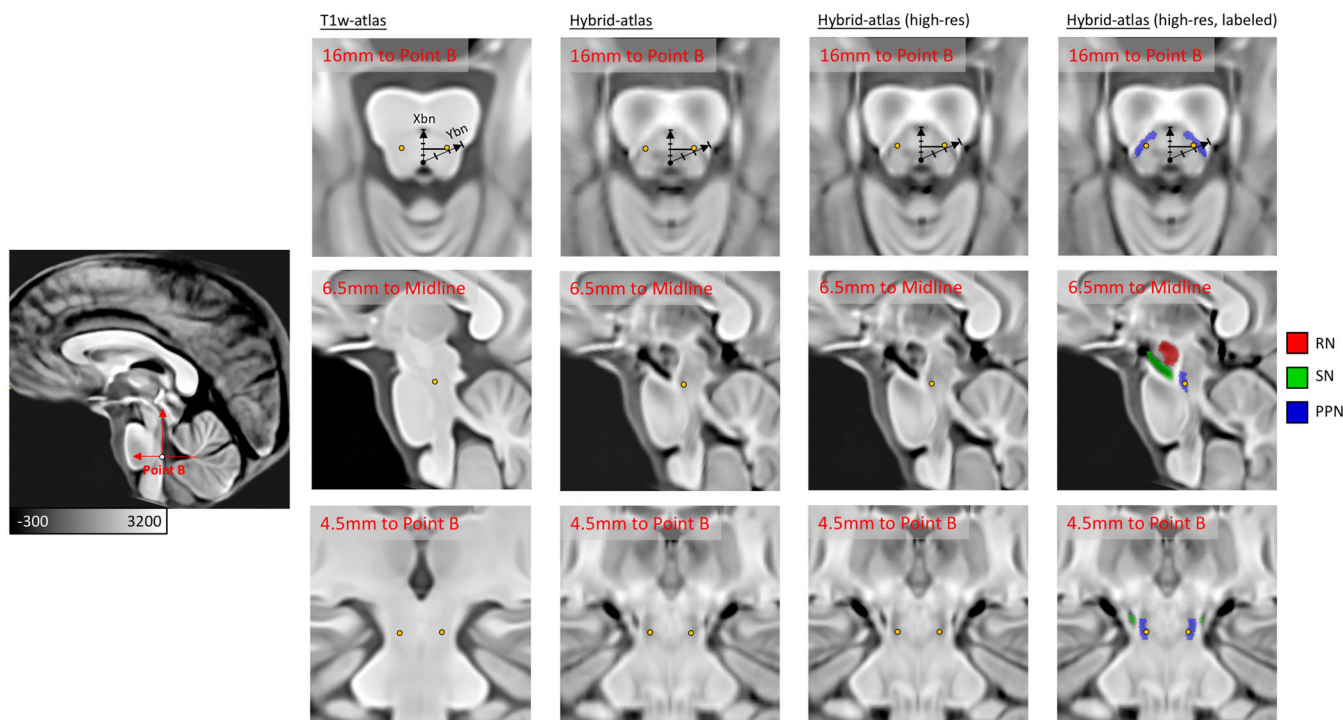
FIGURE 5 The location of the proposed optimal target for PPN-DBS is indicated in our hybrid atlas. The proposed optimal targeting location of PPN-DBS (Goetz et al., 2019) is indicated by the yellow dots on the T1w, hybrid atlas before interpolation, and high-resolution (HR) hybrid atlas. The label of the PPN region (in blue) is overlaid on the HR hybrid atlas in the right column. PPN, pedunculopontine nucleus; RN, red nucleus; SN, substantia nigra, Xbn, brainstem normalized laterality; Ybn, brainstem normalized antero-posteriority.

and 0.096 ± 0.013, respectively, in the T1w, T2w, QSM, and hybrid images of the PD patients. The ratios on the QSM and hybrid images are significantly larger than those on the T1w and T2w images ($p < .01$) (Figure 7b), confirming that the aligned PPN region by registration is more delineable on the QSM and hybrid images.

4 | DISCUSSION

In the present study, we first provide a clear depiction of PPN on the HR T1w-QSM hybrid atlas by fusing the up-sampled MuSus-100 T1w and QSM atlases. Furthermore, the optimal targeting site of PPN-DBS proposed by a recent study is validated at the middle-to-caudal part of PPN on our atlas. Additionally, we demonstrate that the PPN could be directly identified in the individuals' QSM images of PD patients and healthy young adults. Compared with commonly used T1w and T2w images for DBS surgery planning, QSM, and hybrid images significantly improve the contrast ratio of PPN compared to its surrounding brainstem tissues, suggesting that direct targeting of PPN using QSM-based images is feasible in DBS surgery.

4.1 | The proposed SR model for image up-sampling

Without using any HR-low resolution (HR-LR) image training pairs, the proposed self-supervised SR model trained a continuous implicit

function $\widehat{I}_{hr}(\boldsymbol{p})$ to approach the discrete LR image and to synthesize an HR image that follows the continuous assumption of the implicit function. Since only the LR image intensities are involved in the network training, the prior information for the SR process is as limited as that used for 3D image interpolations. Thus, we compare the HR image generation performance of our SR model with the trilinear and sinc interpolation methods. The HR model performs better than the conventional 3D interpolation methods, with fewer blocking artifacts and blurring effects. Using this limited data, the proposed SR should be able to generate a truthful HR template. We provide a HR delineation of the small region of PPN using this method, and the HR QSM atlas may help to delineate other desired small deep brain structures in future studies.

4.2 | A clear delineation of PPN on QSM-based atlas

The structural and connectivity deficits of PPN are associated with gait impairment in PD (Canu et al., 2015; Joza et al., 2022), and the PPN is a potentially effective target for the treatment of DBS for PD, particularly effective in relieving levodopa-refractory axial symptoms such as gait and balance impairment (Galazky et al., 2018; Thevathasan et al., 2018). However, until recently, most PPN-DBS surgeries depended on the indirect targeting method, that is, proportional calculation schemata (Goetz et al., 2019). Direct targeting can improve the targeting accuracy of the neurosurgery (Fenoy & Schiess, 2018; Tonge et al., 2016).
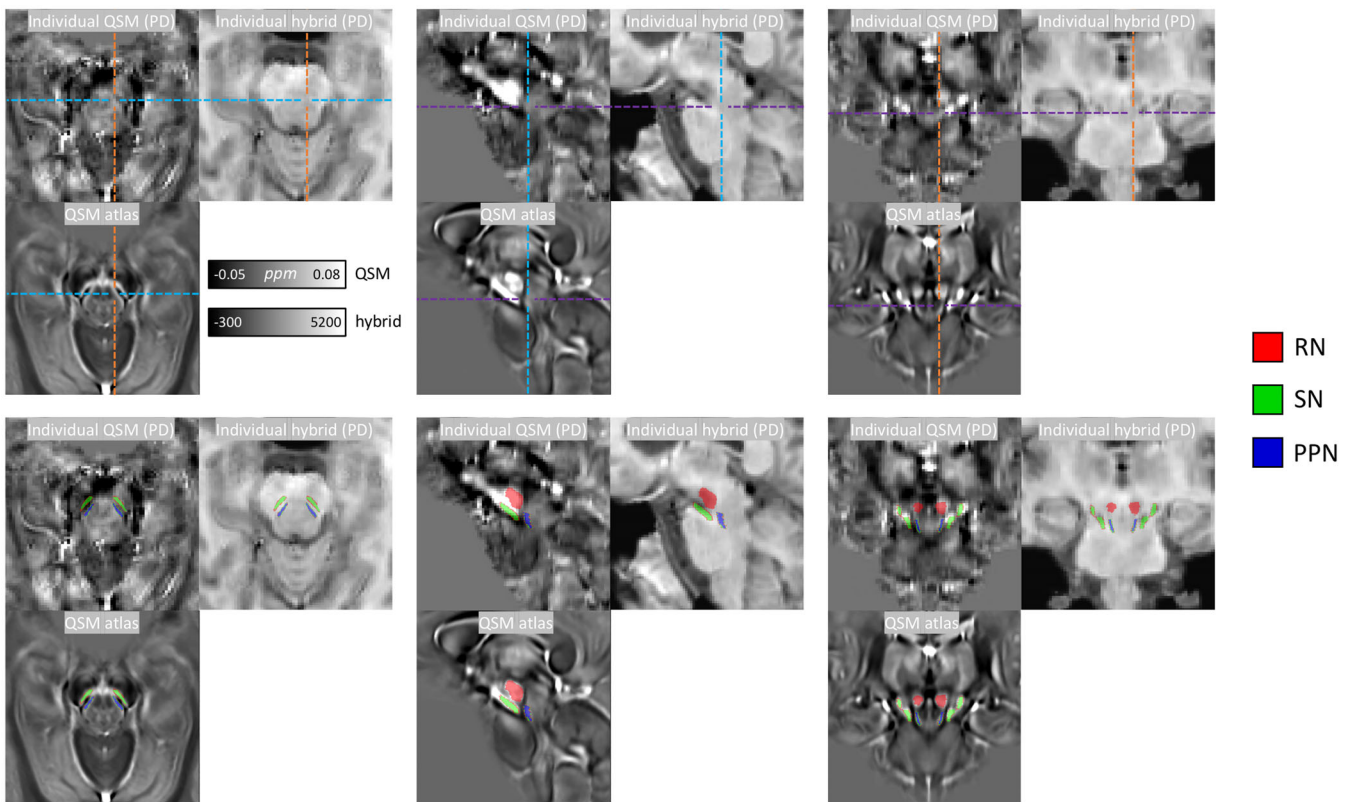
FIGURE 6 Slice views of the PPN region on QSM and hybrid images of a representative PD patient. Slice views containing the PPN region of a representative PD patient are presented with the QSM atlas registered to them. The labels of the PPN region, substantia nigra, and red nucleus, registered to the individual images, are overlaid on the images in the lower panels. ppm, parts per million; PPN, pedunculopontine nucleus; QSM, quantitative susceptibility mapping; RN, red nucleus; SN, substantia nigra.
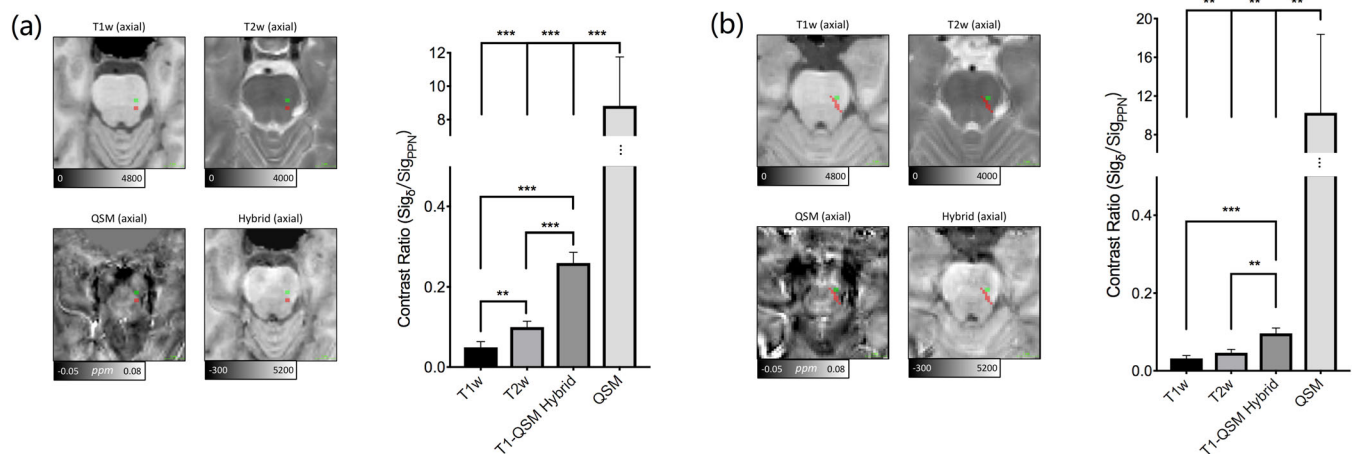

FIGURE 7 Comparison of the contrast ratios of the PPN region and its surrounding structure of medial lemniscus among the images with different modalities. (a) The signal values of the nuclei are extracted as the average values of the manually defined regions (red for PPN and green for medial lemniscus). The contrast ratio is defined as the difference between the signal intensity of PPN and the adjacent medial lemniscus versus the signal intensity of PPN. (b) The contrast ratio of the aligned PPN region (in red) and the manually defined structure of the medial lemniscus (in green). **, $p < .01$; ***, $p < .001$. QSM, quantitative susceptibility mapping; T1w, T1-weighted; T2w, T2-weighted.

We delineate the PPN and identify its surrounding structures on the HR T1w-QSM hybrid atlas. We also identify the optimal targeting site using the proposed coordinates (Goetz et al., 2019) on our hybrid

atlas and validate that the proposed optimal targeting site is located at the middle-to-caudal and posterior part of the PPN region (Figure 5). Furthermore, the aligned PPN region on the individual
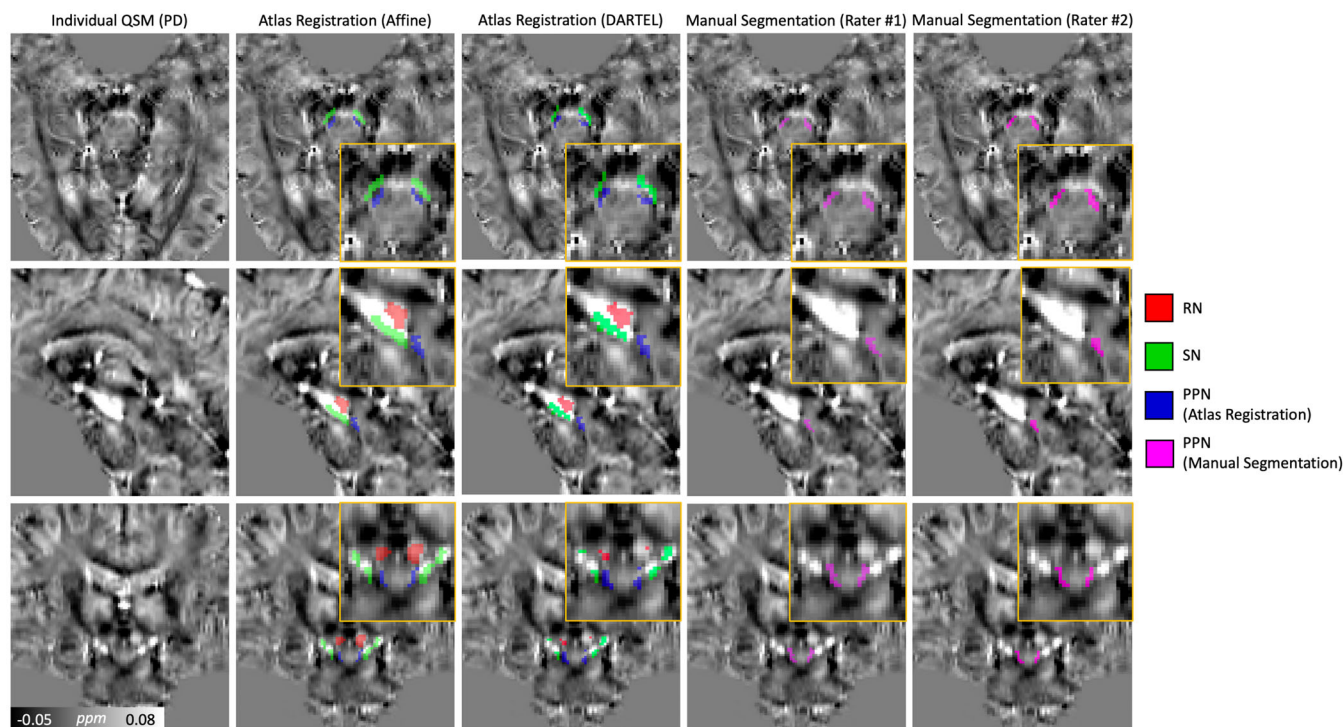
FIGURE 8 Comparison of aligned PPN region and manually segmented PPN region in a representative PD patient. The PPN region identified by registration of the T1w atlas and the individual T1w image is colored in blue. The PPN region manually segmented by two radiologists is colored in lavender. See text for group results. An enlarged view of the PPN region is in the orange box overlaid on the view of the whole brain. DARTEL, Diffeomorphic Anatomical Registration Through Exponentiated Lie Algebra; ppm, parts per million; PPN, pedunculopontine nucleus; QSM, quantitative susceptibility mapping; RN, red nucleus; SN, substantia nigra.

space was confirmed on the individuals' QSM images. This may facilitate more accurate targeting in the PPN-DBS surgery. Since there may be anatomical variations between individuals, the DBS targeting based on coordinates could occasionally be imprecise. The illustration of the structure of the optimal PPN-DBS targets provides a direct visual reference for the neurosurgeons to confirm the targeting based on stereotactic coordinates. Using the PPN label, it is also possible to study the relationship between the stimulation-influenced anatomical location of the PPN and the clinical efficacy of DBS.

4.3 | Identification of PPN on individual images

In this study, the PPN is delineated from its surrounding brainstem structures, namely the medial lemniscus and the decussation SCP in individuals' QSM and hybrid images, indicating the highly differentiated susceptibility of these structures. In contrast, the delineation of PPN from its surrounding structures is not achievable even on the group-averaged T1w template. We also validate that the approximate PPN location can be visually identified in individual QSM images, suggesting that the QSM image may help directly target patient-specific PPN coordinates in the DBS surgeries. Future studies are recommended to confirm whether the QSM technique can improve PPN-DBS effectiveness more than indirect targeting methods in a patient population.

4.4 | Limitations

There are a few limitations to this study. First, the 3D GRE sequence is quite sensitive to patients' motion during scanning, and thus the application in PD patients with obvious tremor might be limited. Secondly, the scanning process for whole-brain GRE images takes nearly 10 minutes, and the generation of QSM images needs post-processing after the GRE images are acquired. Thus, more rapid QSM techniques are yet to be invented for DBS targeting in clinical applications. Thirdly, we delineate the PPN regions merely based on the QSM and T1w-QSM hybrid images, lacking the confirmation of the surrounding WM fiber system. Future studies are needed to confirm that the PPN region identified by QSM has the structural or functional connectivity this nucleus should have. Lastly, it is worth mentioning that having the radiologists segment the PPN region on the individual QSM images may not guarantee perfectly precise segmentation even with the proposed methodology, as this area is difficult to delineate, especially when the image resolution is not high enough.

5 | CONCLUSION

Our findings indicate that the proposed SR network is an efficient tool for small-size brain nucleus identification, and QSM is a promising technique for improving the visibility of the PPN. PPN can be

delineated on the HR QSM-based atlases and identified on the individual QSM images acquired on a 3.0-T MRI scanner, suggesting that the QSM image may help directly target patient-specific PPN coordinates in the DBS surgeries. The HR T1w-QSM atlas and the PPN label are provided to identify the approximate location of PPN via template-image registration when the individual QSM images are unavailable in clinical practice.

AUTHOR CONTRIBUTIONS

Jun Li, Xiaojun Guan, Qing Wu, Chunlei Liu, and Yuyao Zhang conceived the experiment. Jun Li, Weimin Zhang, and Qing Wu performed template generation and image registration. Jun Li, Xiaojun Guan, and Xiaojun Xu performed PPN segmentation. Jun Li, Chenyu He, Xiyue Lin, Hongjiang Wei, and Chunlei Liu performed the data analysis. Jun Li, Xiaojun Xu, Qing Wu, Hongjiang Wei, and Yuyao Zhang drafted the manuscript. Xiaojun Xu and Yuyao Zhang supervised the project. All authors edited and approved the final version of the manuscript.

FUNDING INFORMATION

CONFLICT OF INTEREST STATEMENT

The authors declare that this study was conducted without any commercial or financial relationships that could be construed as a potential conflict of interest.

DATA AVAILABILITY STATEMENT

Data availability statementThe code of the super-resolution model is available at: https://github.com/SMILE-Lab-ShanghaiTech/Human-Pedunculopontine-Nucleus-Atlas. This link also contains the high-resolution T1w, QSM, and T1w-QSM hybrid templates derived from MuSus-100 atlases, as well as the manually delineated label of the pedunculopontine nucleus region. The MRI datasets of PD patients and healthy young adults can be obtained from the corresponding authors upon reasonable request.

ORCID

Jun Li https://orcid.org/0000-0002-4589-7371
Chenyu He https://orcid.org/0000-0003-2730-4437
Xiaojun Xu https://orcid.org/0000-0002-0127-2812

REFERENCES

Alho, A., Hamani, C., Alho, E. J. L., da Silva, R. E., Santos, G. A. B., Neves, R. C., Carreira, L. L., Araújo, C. M. M., Magalhães, G., Coelho, D. B., Alegro, M. C., Martin, M. G. M., Grinberg, L. T., Pasqualucci, C. A., Heinsen, H., Fonoff, E. T., & Amaro, E., Jr. (2017). Magnetic resonance diffusion tensor imaging for the pedunculopontine nucleus: Proof of concept and histological correlation. *Brain Structure & Function*, *222*(6), 2547–2558. https://doi.org/10.1007/s00429-016-1356-0

Alkemade, A., de Hollander, G., Keuken, M. C., Schafer, A., Ott, D. V. M., Schwarz, J., Weisi, D., Kotz, S. A., & Forstmann, B. U. (2017). Comparison of T2*-weighted and QSM contrasts in Parkinson's disease to visualize the STN with MRI. *PLoS One*, *12*(4), e0176130. https://doi.org/10.1371/journal.pone.0176130

Andres, P., & Isoardi, R. (2007). Using ITK platform for medical image registration. *Journal of Physics: Conference Series*, *90*(1), 012056. https://doi.org/10.1088/1742-6596/90/1/012056

Aravamuthan, B. R., Muthusamy, K. A., Stein, J. F., Aziz, T. Z., & Johansen-Berg, H. (2007). Topography of cortical and subcortical connections of the human pedunculopontine and subthalamic nuclei. *NeuroImage*, *37*(3), 694–705. https://doi.org/10.1016/j.neuroimage.2007.05.050

Ashburner, J. (2007). A fast diffeomorphic image registration algorithm. *NeuroImage*, *38*(1), 95–113. https://doi.org/10.1016/j.neuroimage.2007.07.007

Canu, E., Agosta, F., Sarasso, E., Volonte, M. A., Basaia, S., Stojkovic, T., Stefanova, E., Comi, G., Falini, A., Kostic, V. S., Gatti, R., & Filippi, M. (2015). Brain structural and functional connectivity in Parkinson's disease with freezing of gait. *Human Brain Mapping*, *36*(12), 5064–5078. https://doi.org/10.1002/hbm.22994

Cong, F., Wang, J. W., Wang, B., Yang, Z., An, J., Zuo, Z., Zhang, Z., Zhang, Y.-Q., & Zhuo, Y. (2018). Direct localisation of the human pedunculopontine nucleus using MRI: A coordinate and fibre-tracking study. *European Radiology*, *28*(9), 3882–3892. https://doi.org/10.1007/s00330-017-5299-5

Cury, R. G., Pavese, N., Aziz, T. Z., Krauss, J. K., Moro, E., & Neuromodulation of Gait Study Group from Movement Disorders Society. (2022). Gaps and roadmap of novel neuromodulation targets for treatment of gait in Parkinson's disease. *NPJ Parkinsons Dis*, *8*(1), 8. https://doi.org/10.1038/s41531-021-00276-6

Dayal, V., Rajabian, A., Jahanshahi, M., Aviles-Olmos, I., Cowie, D., Peters, A., Day, B., Hyam, J., Akram, H., Limousin, P., Hariz, M., & Foltynie, T. (2021). Pedunculopontine nucleus deep brain stimulation for parkinsonian disorders: A case series. *Stereotactic and Functional Neurosurgery*, *99*(4), 287–294. https://doi.org/10.1159/000511978

Dimov, A. V., Gupta, A., Kopell, B. H., & Wang, Y. (2018). High-resolution QSM for functional and structural depiction of subthalamic nuclei in DBS presurgical mapping. *Journal of Neurosurgery*, *1-8*, 360–367. https://doi.org/10.3171/2018.3.JNS172145

Fenoy, A. J., & Schiess, M. C. (2018). Comparison of tractography-assisted to atlas-based targeting for deep brain stimulation in essential tremor. *Movement Disorders*, *33*(12), 1895–1901. https://doi.org/10.1002/mds.27463

Galazky, I., Kaufmann, J., Lorenzl, S., Ebersbach, G., Gandor, F., Zaehle, T., Specht, S., Stallforth, S., Sobieray, U., Wirkus, E., Casjens, F., Heinze, H.-J., Kupsch, A., & Voges, J. (2018). Deep brain stimulation of the pedunculopontine nucleus for treatment of gait and balance disorder in progressive supranuclear palsy: Effects of frequency modulations and clinical outcome. *Parkinsonism & Related Disorders*, *50*, 81–86. https://doi.org/10.1016/j.parkreldis.2018.02.027

Garcia-Gomar, M. G., Singh, K., Cauzzo, S., & Bianciardi, M. (2022). In vivo structural connectome of arousal and motor brainstem nuclei by 7 tesla and 3 tesla MRI. *Human Brain Mapping*, *43*, 4397–4421. https://doi.org/10.1002/hbm.25962

Goetz, L., Bhattacharjee, M., Ferraye, M. U., Fraix, V., Maineri, C., Nosko, D., Fenoy, A. J., Piallat, B., Torres, N., Krainik, A., Seigneuret, E., David, O., Parent, M., Parent, A., Pollak, P., Benabid, A.-L., Debu, B., & Chabardes, S. (2019). Deep brain stimulation of the pedunculopontine nucleus area in Parkinson disease: MRI-based Anatomoclinical correlations and optimal target. *Neurosurgery*, *84*(2), 506–518. https://doi.org/10.1093/neuros/nyy151

Hamani, C., Aziz, T., Bloem, B. R., Brown, P., Chabardes, S., Coyne, T., Foote, K., Garcia-Rill, E., Hirsch, E. C., Lozano, A. M., Mazzone, P. A. M., Okun, M. S., Hutchison, W., Silburn, P., Zrinzo, L., Alam, M., Goetz, L., Pereira, E., Rughani, A., … Krauss, J. K. (2016).

Pedunculopontine nucleus region deep brain stimulation in Parkinson disease: Surgical anatomy and terminology. *Stereotactic and Functional Neurosurgery*, *94*(5), 298–306. https://doi.org/10.1159/000449010

He, C., Guan, X., Zhang, W., Li, J., Liu, C., Wei, H., Xu, X., & Zhang, Y. (2022). Quantitative susceptibility atlas construction in Montreal neurological institute space: Towards histological-consistent iron-rich deep brain nucleus subregion identification. *Brain Structure & Function*. Online ahead of print. https://doi.org/10.1007/s00429-022-02547-1

He, N., Langley, J., Huddleston, D. E., Ling, H., Xu, H., Liu, C., Yan, F., & Hu, X. P. (2017). Improved neuroimaging atlas of the dentate nucleus. *Cerebellum*, *16*(5–6), 951–956. https://doi.org/10.1007/s12311-017-0872-7

Jenkinson, N., Nandi, D., Muthusamy, K., Ray, N. J., Gregory, R., Stein, J. F., & Aziz, T. Z. (2009). Anatomy, physiology, and pathophysiology of the pedunculopontine nucleus. *Movement Disorders*, *24*(3), 319–328. https://doi.org/10.1002/mds.22189

Joza, S., Camicioli, R., Martin, W. R. W., Wieler, M., Gee, M., & Ba, F. (2022). Pedunculopontine nucleus dysconnectivity correlates with gait impairment in Parkinson's disease: An exploratory study. *Frontiers in Aging Neuroscience*, *14*, 874692. https://doi.org/10.3389/fnagi.2022.874692

Kerl, H. U., Gerigk, L., Pechlivanis, I., Al-Zghloul, M., Groden, C., & Nolte, I. (2012). The subthalamic nucleus at 3.0 tesla: Choice of optimal sequence and orientation for deep brain stimulation using a standard installation protocol: Clinical article. *Journal of Neurosurgery*, *117*(6), 1155–1165. https://doi.org/10.3171/2012.8.JNS111930

Leiras, R., Cregg, J. M., & Kiehn, O. (2022). Brainstem circuits for locomotion. *Annual Review of Neuroscience*, *45*, 63–85. https://doi.org/10.1146/annurev-neuro-082321-025137

Li, J., Li, Y., Gutierrez, L., Xu, W., Wu, Y., Liu, C., Li, D., Sun, B., Zhang, C., & Wei, H. (2019). Imaging the Centromedian thalamic nucleus using quantitative susceptibility mapping. *Frontiers in Human Neuroscience*, *13*, 447. https://doi.org/10.3389/fnhum.2019.00447

Li, W., Wu, B., & Liu, C. (2011). Quantitative susceptibility mapping of human brain reflects spatial variation in tissue composition. *NeuroImage*, *55*(4), 1645–1656. https://doi.org/10.1016/j.neuroimage.2010.11.088

Liu, C., Wei, H., Gong, N. J., Cronin, M., Dibb, R., & Decker, K. (2015). Quantitative susceptibility mapping: Contrast mechanisms and clinical applications. *Tomography*, *1*(1), 3–17. https://doi.org/10.18383/j.tom.2015.00136

Liu, T., Eskreis-Winkler, S., Schweitzer, A. D., Chen, W., Kaplitt, M. G., Tsiouris, A. J., & Wang, Y. (2013). Improved subthalamic nucleus depiction with quantitative susceptibility mapping. *Radiology*, *269*(1), 216–223. https://doi.org/10.1148/radiol.13121991

Martin, J. H. (2012). *Neuroanatomy text and atlas*. McGraw-Hill.

Muthusamy, K. A., Aravamuthan, B. R., Kringelbach, M. L., Jenkinson, N., Voets, N. L., Johansen-Berg, H., Stein, H. J.-B., & Aziz, T. Z. (2007). Connectivity of the human pedunculopontine nucleus region and diffusion tensor imaging in surgical targeting. *Journal of Neurosurgery*, *107*(4), 814–820. https://doi.org/10.3171/JNS-07/10/0814

Pahapill, P. A., & Lozano, A. M. (2000). The pedunculopontine nucleus and Parkinson's disease. *Brain*, *123*(Pt 9), 1767–1783. https://doi.org/10.1093/brain/123.9.1767

Schindelin, J., Arganda-Carreras, I., Frise, E., Kaynig, V., Longair, M., Pietzsch, T., Preibisch, S., Rueden, C., Saalfeld, S., Schmid, B., Tinevez, J.-Y., White, D. J., Hartenstein, V., Eliceiri, K., Tomancak, P., & Cardona, A. (2012). Fiji: An open-source platform for biological-image analysis. *Nature Methods*, *9*(7), 676–682. https://doi.org/10.1038/nmeth.2019

Schweser, F., Deistung, A., Lehr, B. W., & Reichenbach, J. R. (2011). Quantitative imaging of intrinsic magnetic tissue properties using MRI signal phase: An approach to in vivo brain iron metabolism? *NeuroImage*, *54*(4), 2789–2807. https://doi.org/10.1016/j.neuroimage.2010.10.070

Shmueli, K., de Zwart, J. A., van Gelderen, P., Li, T. Q., Dodd, S. J., & Duyn, J. H. (2009). Magnetic susceptibility mapping of brain tissue in vivo using MRI phase data. *Magnetic Resonance in Medicine*, *62*(6), 1510–1522. https://doi.org/10.1002/mrm.22135

Sun, H., Walsh, A. J., Lebel, R. M., Blevins, G., Catz, I., Lu, J. Q., Johnson, E. S., Emery, D. J., Warren, K. G., & Wilman, A. H. (2015). Validation of quantitative susceptibility mapping with Perls' iron staining for subcortical gray matter. *NeuroImage*, *105*, 486–492. https://doi.org/10.1016/j.neuroimage.2014.11.010

Tancik, M., Srinivasan, P. P., Mildenhall, B., Fridovich-Keil, S., Raghavan, N., Singhal, U., Ramamoorthi, R., Barron, J. T., & Ng, R. (2020). Fourier features let networks learn high frequency functions in low dimensional domains. *Advances in Neural Information Processing Systems*, *33*, 7537–7547. https://doi.org/10.48550/arXiv.2006.10739

Thevathasan, W., Debu, B., Aziz, T., Bloem, B. R., Blahak, C., Butson, C., Czernecki, V., Foltynie, T., Fraix, V., Grabli, D., Joint, C., Lozano, A. M., Okun, M. S., Ostrem, J., Pavese, N., Schrader, C., Tai, C.-H., Krauss, J. K., Moro, E., ... Functional, N. (2018). Pedunculopontine nucleus deep brain stimulation in Parkinson's disease: A clinical review. *Movement Disorders*, *33*(1), 10–20. https://doi.org/10.1002/mds.27098

Tonge, M., Kocabicak, E., Ackermans, L., Kuijf, M., & Temel, Y. (2016). Final electrode position in subthalamic nucleus deep brain stimulation surgery: A comparison of indirect and direct targeting methods. *Turkish Neurosurgery*, *26*(6), 900–903. https://doi.org/10.5137/1019-5149.JTN.13739-14.1

Wang, J. W., Cong, F., Zhuo, Y., Chen, L., Wang, B., & Zhang, Y. Q. (2019). 7.0T ultrahigh-field MRI directly visualized the pedunculopontine nucleus in Parkinson's disease patients. *Clinics (São Paulo, Brazil)*, *74*, e573. https://doi.org/10.6061/clinics/2019/e573

Wei, H., Cao, S., Zhang, Y., Guan, X., Yan, F., Yeom, K. W., & Liu, C. (2019). Learning-based single-step quantitative susceptibility mapping reconstruction without brain extraction. *NeuroImage*, *202*, 116064. https://doi.org/10.1016/j.neuroimage.2019.116064

Wei, H., Dibb, R., Zhou, Y., Sun, Y., Xu, J., Wang, N., & Liu, C. (2015). Streaking artifact reduction for quantitative susceptibility mapping of sources with large dynamic range. *NMR in Biomedicine*, *28*(10), 1294–1303. https://doi.org/10.1002/nbm.3383

Wei, H., Zhang, C., Wang, T., He, N., Li, D., Zhang, Y., Liu, C., Yan, F., & Sun, B. (2019). Precise targeting of the globus pallidus internus with quantitative susceptibility mapping for deep brain stimulation surgery. *Journal of Neurosurgery*, *1-7*, 1605–1611. https://doi.org/10.3171/2019.7.JNS191254

Wu, Q., Li, Y., Sun, Y., Zhou, Y., Wei, H., Yu, J., & Zhang, Y. (2023). An arbitrary scale super-resolution approach for 3D MR images via implicit neural representation. *IEEE Journal of Biomedical and Health Informatics*, *27*(2), 1004–1015. https://doi.org/10.1109/JBHI.2022.3223106

Wu, Q., Li, Y., Xu, L., Feng, R., Wei, H., Yang, Q., Yu, B., Liu, X., Yu, J., & Zhang, Y. (2021). *IREM: High-resolution magnetic resonance image reconstruction via implicit neural representation*. Medical Image Computing and Computer Assisted Intervention, MICCAI. pp. 65–74. https://doi.org/10.1007/978-3-030-87231-1_7

Yan, C. G., Wang, X. D., Zuo, X. N., & Zang, Y. F. (2016). DPABI: Data Processing & Analysis for (resting-state) brain imaging. *Neuroinformatics*, *14*(3), 339–351. https://doi.org/10.1007/s12021-016-9299-4

Yu, B., Li, L., Guan, X., Xu, X., Liu, X., Yang, Q., Wei, H., Zuo, C., & Zhang, Y. (2021). HybraPD atlas: Towards precise subcortical nuclei segmentation using multimodality medical images in patients with Parkinson disease. *Human Brain Mapping*, *42*(13), 4399–4421. https://doi.org/10.1002/hbm.25556

Yu, K., Ren, Z., Yu, T., Wang, X., Hu, Y., Guo, S., Li, J., & Li, Y. (2021). Direct targeting of the anterior nucleus of the thalamus via 3 T quantitative susceptibility mapping. *Frontiers in Neuroscience*, *15*, 685050. https://doi.org/10.3389/fnins.2021.685050

Zhang, Y., Wei, H., Cronin, M. J., He, N., Yan, F., & Liu, C. (2018). Longitudinal atlas for normative human brain development and aging over the lifespan using quantitative susceptibility mapping. *NeuroImage*, *171*, 176–189. https://doi.org/10.1016/j.neuroimage.2018.01.008

Zitella, L. M., Xiao, Y., Teplitzky, B. A., Kastl, D. J., Duchin, Y., Baker, K. B., Vitek, J. L., Adriany, G., Yacoub, E., Harel, N., & Johnson, M. D. (2015). In vivo 7T MRI of the non-human primate brainstem. *PLoS One*, *10*(5), e0127049. https://doi.org/10.1371/journal.pone.0127049

Zrinzo, L., Zrinzo, L. V., Tisch, S., Limousin, P. D., Yousry, T. A., Afshar, F., & Hariz, M. I. (2008). Stereotactic localization of the human pedunculopontine nucleus: Atlas-based coordinates and validation of a magnetic resonance imaging protocol for direct localization. *Brain*, *131*(Pt 6), 1588–1598. https://doi.org/10.1093/brain/awn075

SUPPORTING INFORMATION

Additional supporting information can be found online in the Supporting Information section at the end of this article.

How to cite this article: Li, J., Guan, X., Wu, Q., He, C., Zhang, W., Lin, X., Liu, C., Wei, H., Xu, X., & Zhang, Y. (2023). Direct localization and delineation of human pedunculopontine nucleus based on a self-supervised magnetic resonance image super-resolution method. *Human Brain Mapping*, *44*(9), 3781–3794. https://doi.org/10.1002/hbm.26311